Journal of Applied Fluid Mechanics , Vol. 9, No. 3, pp. 1533-1549, 2016.
Available online at www.jafmonline.net, ISSN 1735-3572, EISSN 1735-3645.

Lagrangian Particle Tracking in Velocity-Vorticity Resolved Viscous Flows by Subdomain BEM

J. Ravnik †, M. Hriberšek and J. Lupše

Faculty of Mechanical Engineering, University of Maribor, Smetanova ulica 17, SI-2000 Maribor, Slovenia

† *Corresponding Author Email*: *jure.ravnik@um.si*

(Received Octobr 3, 2013; accepted January 7, 2015)

ABSTRACT

A numerical study of particle motion in a cubic lid driven cavity is presented. As a computational tool, a boundary element based flow solver with a Lagrangian particle tracking algorithm is derived. Flow simulations were performed using an in-house boundary element based 3D viscous flow solver. The Lagrangian particle tracking algorithm is capable of simulation of dilute suspensions of particles in viscous flows taking into account gravity, buoyancy, drag, pressure gradient and added mass. The derived algorithm is used to simulate particle behaviour in a cellular flow field and in a lid driven cavity flow. Simulations of particle movement in a cellular flow field were used to validate the algorithm. The main goal of the paper was to numerically simulate the flow behaviour of spheres of different densities and different diameters, as experimentally observed in work of Tsorng et al.The study of slightly buoyant and non-buoyant particles in a lid driven cavity was aimed at discovering cases when particles leave the primary vortex and enter into secondary vortices, a phenomenon described in the work of Tsorng et al. A parametric study of this phenomenon was preformed. The presented computational results show excellent agreement with experiments, confirming the accuracy of the developed computational method.

Keywords: Dispersed two phase flow; Lagrangian particle tracking; Cellular flow; Lid driven cavity; Boundary element method.

NOMENCLATURE

$\vec{a}$	particle acceleration	$\vec{\omega}$	fluid vorticity
c	boundary element shape parameter	$\vec{v}$	particle velocity
d_p	particle diameter	ρ	fluid density
$\vec{g}$	gravitational acceleration	ρ_p	particle density
$\vec{n}$	unit normal	$\vec{v}_s$	particle settling velocity
$\vec{r}$	particle position	$\vec{\nabla}$	gradient operator
Re	Reynolds number	$\vec{\vartheta}$	source point
St	particle Stokes number	Ω	domain
t	time	$\partial\Omega = \Gamma$	boundary of the domain
$\vec{u}$	fluid velocity	ν	fluid kinematic viscosity
$u^\star$	fundamental solution	τ_p	particle relaxation time

1. INTRODUCTION

Dispersed two phase flows are commonly encountered in environmental flows and engineering practice, especially in process engineering. Environmental flows commonly include dispersion of solid or liquid particles in atmosphere and solid, liquid and gas particles in hydrosphere. In process engineering, the main attraction of implementing dispersed multiphase flow systems is in a large contact area between the continuous and dispersed phase, thus increasing the effective heat and mass transport between particles and fluid. On the other hand, dispersed multiphase systems arise in pneumatic and slurry transport systems, enabling effective transportation of granular material inside a pro-

cess system, as well as inside chemical reactors, as for example in crystallization and extraction processes (Crowe 1998). In the latter case, mixing vessel with Rushton impellers is a frequently encountered process equipment. A simplification of such a system is a driven cavity flow in a cubic cavity. Existence of recirculation areas in corners of the cavity can effect the quality of the product, as these areas posses characteristics of low heat and mass transfer. It is therefore an important question, when and how do particles of various sizes and densities enter these areas.

In order to accurately describe hydrodynamics of such flows, forming the basis for description of heat and mass transfer between the dispersed and continuous phase, one has several options, see for example van Wachem and Almstedt (2003) or Mendez (2011). The options, that are linked to CFD resolution of continuous phase and are computationally affordable for engineering community, are:

- The first relies on assumption, that the system can be described as quasi homogeneous with suitably chosen material properties, e.g. average density, effective viscosity, thermal conductivity and mass diffusion. The resulting system of equations is easy to solve by means of standard (single phase) CFD tools, however, the results are rarely very accurate. An example is the work of Necker *et al.* (2002), where a sedimentation velocity approach was coupled with an additional transport equation for dispersed phase concentration.

- The second relies on assumption, that the dispersed phase can be modelled as a continuous phase, with some artificial physical properties (e.g. solid phase viscosity). Again, the standard single phase tools can be used, this time for each phase separately, and interaction between the phases additionally has to be modelled. Typical examples include Euler-Euler simulations, see Sachdev *et al.* (2007). In this case, a detailed study of particle movement is not possible, since the particles are simulated as a continuous phase. Volume of fluid method is also an example of Eulerian two-phase flow simulation tool. Razmi *et al.* (2009) have considered unsteady two-phase finite volume method with volume of fluid) model to study settling tanks.

- The third option relies on simulation of dispersed phase as a numerical tracking of particles in the moving fluid. The computationally most affordable approach is description of a particle as a rigid sphere, that interacts with fluid phase, and also occupies the same volume as fluid. The continuous phase is computed by means of a standard CFD approach. The so called Lagrangian particle tracking has a superior spatial accuracy, and allows different phenomena to be accurately modelled and computed, e.g. heat and mass transfer from the particles, accurate incorporation of drag and lift forces. Works include the finite difference, finite element and finite volume based algorithms (Patankar and Joseph 2001; Tamayol, Firoozabadi, and Ahmadi 2008).

Physically more realistic models also exist, such as where particles do not occupy the same volume as fluid. These approaches are computationally demanding and are not considered in the present work. Instead, in the present work, the third option is implemented. As a starting point, the earlier work by Ravnik *et. al* (2008) was chosen, where a BEM-FEM algorithm for a 2D flow simulation was coupled by explicit Lagrangian particle tracking algorithm, but the interaction between particles and the fluid was modelled by simple sedimentation velocity approach. In order to realistically capture the particle response to fluid flow structures, full one-way coupling was implemented in the present work. The particles move due to the action of gravity, buoyancy, drag, pressure gradient and added mass forces in a 3D flow field. Since numerical simulation of dilute suspensions is the main target of this work, the coupling between the two phases is a one-way action of fluid on to particle. One of the main challenges in numerical simulation of the described flows is also a capability to accurately predict flows of particles with densities, that are very close to density of the fluid phase.

Maxey (1987) studied the motion of small spherical particles in a cellular flow field, examining the behaviour of particles having a wide range of densities. The work of Maxey was chosen to serve as a benchmark for testing the accuracy of the developed particle tracking algorithm. As a second example the particle movement in a lid driven cavity flow is selected. The case was experimentally studied by Tsorng *et al.* (2008) and offers an excellent combination of a standard benchmark test case for fluid flow with praxis relevant study of particle movement in the flow. The practical aspects refer to

flow in various mixing devices.

The paper is organized as follows. First, a short description of the approximation boundary element method (BEM) for the solution of fluid flow field is given and flow simulations are presented. This is followed by an extensive description of the Lagrangian particle simulation method. The Lagrangian solver is validated on the test case of particle movement in a predefined cellular flow. The main part of the paper is devoted to numerical simulations of movement of particles of various sizes and densities in the lid driven cavity flow. The paper concludes with the analysis of entrainment of particles into secondary vortices, formed in lid driven cavity flows.

2. SIMULATION OF FLUID FLOW

Laminar viscous flow was simulated using an in-house code based on Ravnik *et al.* (2008). The code solves the velocity-vorticity formulation of Navier-Stokes equations using the boundary-domain integral method. A combination of sub-domain and single domain technique is used. Incompressible viscous Newtonian fluid with constant material properties is considered. In velocity-vorticity formulation vorticity $\vec{\omega}$ is defined as the curl of the velocity $\vec{\omega} = \vec{\nabla} \times \vec{u}$. Both velocity and vorticity fields are divergence free. The viscous fluid flow is governed by the kinematics equation

$$\nabla^2 \vec{u} + \vec{\nabla} \times \vec{\omega} = 0, \tag{1}$$

which links the velocity and vorticity fields for every point in space and time. The kinetic aspect of fluid movement is governed by the vorticity transport equation, written in non-dimensional form:

$$\frac{\partial \vec{\omega}}{\partial t} + (\vec{u} \cdot \vec{\nabla})\vec{\omega} = (\vec{\omega} \cdot \vec{\nabla})\vec{u} + \frac{1}{Re}\nabla^2 \vec{\omega}, \tag{2}$$

with the Reynolds number denoted by *Re*. Equation (2) equates the advective vorticity transport on the left hand side with the vortex twisting and stretching term and the diffusion term on the right hand side.

The system of equations (1) and (2) is solved in a nonlinear loop of three steps. In the first step, boundary vorticity values are calculated by solving the kinematics equation by single domain BEM. The second step is the calculation of domain velocity values by solving the kinematics equation by subdomain BEM and the final step is the solution of vorticity transport equation for domain vorticity values using the boundary values from the solution of the kinematics equation by subdomain BEM.

The boundary condition required to obtain the solution is the prescribed velocity on the boundary. The unknown boundary conditions for the vorticity transport equation are calculated as a part of the algorithm using single domain BEM.

2.1 Integral Form of Governing Equations

2.11 The kinematics equation

In the subdomain BEM approach the whole domain Ω is divided into subdomains Ω_i, where $\sum \Omega_i = \Omega$. The boundary of each subdomain is denoted by $\partial\Omega_i$. The integral form of the kinematics equation without derivatives of the velocity and vorticity fields takes the following form:

$$c(\vec{\vartheta})\vec{u}(\vec{\vartheta}) + \int_{\partial\Omega_i} \vec{u}\vec{\nabla}u^\star \cdot \vec{n} d\Gamma = \int_{\partial\Omega_i} \vec{u} \times (\vec{n} \times \vec{\nabla})u^\star d\Gamma + \int_{\Omega_i} (\vec{\omega} \times \vec{\nabla}u^\star) d\Omega, \tag{3}$$

where $\vec{r}$ is the location point, $\vec{\vartheta}$ is the source or collocation point, $\vec{n}$ is the unit normal to the boundary and $u^\star = 1/4\pi|\vec{\vartheta} - \vec{r}|$ is the fundamental solution of the Laplace operator. $c(\vec{\vartheta})$ is the geometric factor defined as $c(\vec{\vartheta}) = \alpha/4\pi$, where α is the inner angle with origin in $\vec{\vartheta}$. Solution of this equation is used in the second step of the algorithm to obtain domain velocity values.

2.12 The vorticity transport equation

The solution of the vorticity transport equation yields the flow vorticity as a part of the solution, which is an advantage when tracking particle in vorticity dominated flows, as the need for numerical differentiation is omitted.

The integral form of the steady vorticity transport equation (2) may be written for the j^{th} component of the vorticity vector as:

$$c(\vec{\vartheta})\omega_j(\vec{\vartheta}) + \int_{\partial\Omega_i} \omega_j \vec{\nabla}u^* \cdot \vec{n} d\Gamma = \int_{\partial\Omega_i} u^* q_j d\Gamma + Re \int_{\partial\Omega_i} \vec{n} \cdot \left\{ u^* (\vec{v}\omega_j - \vec{\omega}u_j) \right\} d\Gamma - Re \int_{\Omega_i} (\vec{u}\omega_j - \vec{\omega}u_j) \cdot \vec{\nabla}u^* d\Omega, \tag{4}$$

where ω_j is the j-th component of the velocity vector and $\vec{q}$ is the vorticity flux vector $q_j = \vec{n} \cdot \vec{\nabla}\omega_j$. Solution of the vorticity transport equations yields domain vorticity values in the final step of the algorithm.

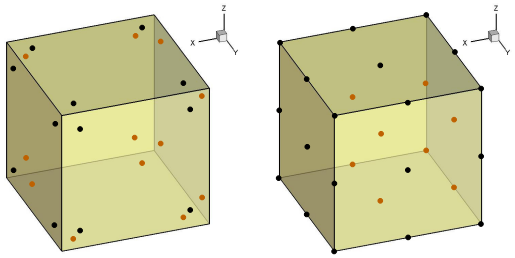

Fig. 1. Node locations in a hexahedral element for quadratic interpolation of function (right) and linear interpolation of flux (left). The same locations are used for source points, when assembling the system of linear equations.

The field functions and fluxes as well as the products of velocity and vorticity field components are interpolated within hexahedral elements using shape functions (Figure 1).

In order to set up a system of equations the source point is set in all function and flux nodes of all mesh elements. Each element is treated as an individual subdomain, thus a sparse system of equations is obtained. Compatibility boundary conditions are employed between subdomains. The sparse system of equations is solved using least squares based iterative solver (Paige and Saunders 1982).

2.13 The kinematics equation for boundary vorticity

In order to use the kinematics equation to obtain boundary vorticity values, we rewrite the equation (3) into a tangential form by multiplying the system with a normal in the source point:

$$c(\vec{\vartheta})\vec{n}(\vec{\vartheta})\times\vec{u}(\vec{\vartheta})+\vec{n}(\vec{\vartheta})\times\int_{\partial\Omega}\vec{u}\vec{\nabla}u^{\star}\cdot\vec{n}d\Gamma= \vec{n}(\vec{\vartheta})\times\int_{\partial\Omega}\vec{u}\times(\vec{n}\times\vec{\nabla})u^{\star}d\Gamma+ \vec{n}(\vec{\vartheta})\times\int_{\Omega}(\vec{\omega}\times\vec{\nabla}u^{\star})d\Omega. \quad (5)$$

This approach has been proposed by Škerget and used in 2D by Škerget *et al.* (2003).

The source point is set in all nodes on the exterior boundary of the domain. This leads to a system of linear equations for boundary vorticity values. The solution of this system is computed in each iteration of the nonlinear solution process until convergence is achieved. Since the system matrix remains unchanged through the whole nonlinear solution procedure, i.e. it does not depend on the flow variables, we perform the LU decomposition on the system matrix before the start of the nonlinear loop. Then, in each iteration of the nonlinear loop, the stored LU decomposition is used to obtain the boundary vorticity values.

2.2 Flow in a Lid Driven Cavity

In the lid driven cavity, the moving top lid induces a large primary vortex in the centre of a cubical enclosure. The size of the vortex increases with Reynolds number. Secondary vortices appear in the corners of the cavity, their position and strength changing with Reynolds number. Figure 2 shows the boundary conditions of the lid driven cavity graphically. The Reynolds number for this case is defined with the length of cavity's edge L and the top wall velocity u_0. The particle experiments preformed by Tsorng *et al.* (2008) were done at $Re = 130$, $Re = 470$ and $Re = 860$, thus we simulated the flow at these conditions.

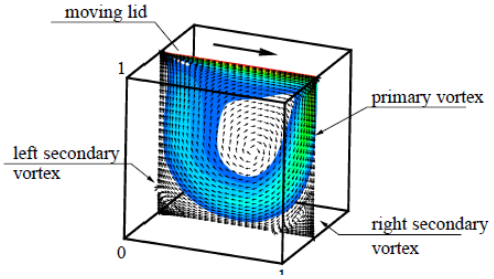

Fig. 2. Geometry and boundary conditions of the lid driven cavity test case. The top wall is moving, the fluid does not slip on any wall.

In Ravnik *et al.* (2009) we reported that a 33^3 mesh with nodes concentrated towards the corners, is sufficient for simulation of lid driven cavity flow up to $Re = 1000$. Thus, we decided to use the 33^3 mesh to simulate all flow fields.

To visualize the flow fields, we present isosurfaces of the velocity field in Figure 3. As the Reynolds number increases the size of the primary vortex in the cavity also increases. At $Re = 860$ it fills up almost the entire cavity, keeping secondary vortices in lower corners. The absolute vorticity value plots on the isosurfaces of velocity show regions of high vorticity values, where particles experience considerable rotational influences from the fluid side, as established in experiments of Tsorng *et al.* (2008).

Additionally, Figure 4 shows velocity profiles through the centrelines of the cavity. We observe that along with the increase of the primary vortex with Reynolds number, the veloci-

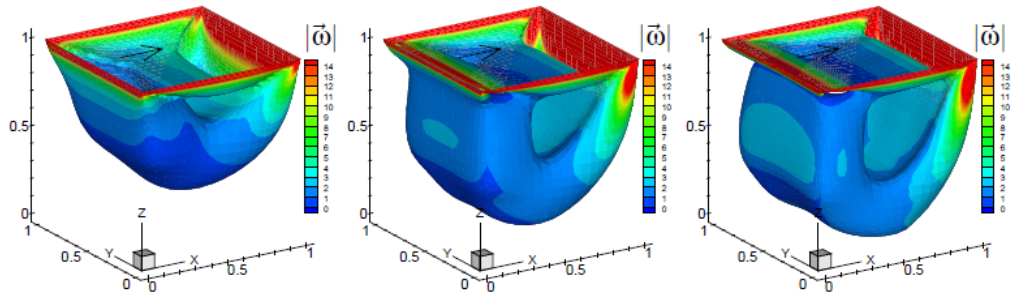

Fig. 3. Isosurfaces of velocity $|\vec{u}| = 0.14$ contoured with absolute value of vorticity $|\vec{\omega}|$. Top left $Re = 130$, top right $Re = 470$ and bottom $Re = 860$. Moving lid direction is shown with an arrow.

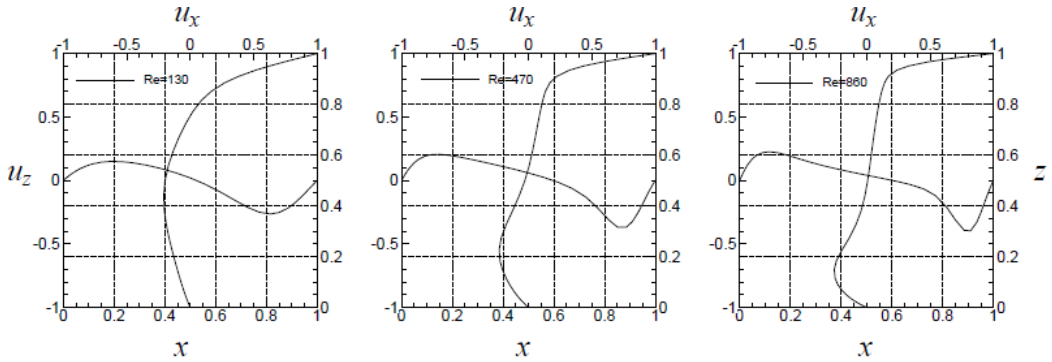

Fig. 4. Velocity profiles through the $y = 0.5$ plane in the lid driven cavity test case. Left $Re = 130$, middle $Re = 470$ and right $Re = 860$.

ties, throughout the cavity are increased as well.

3. LAGRANGIAN PARTICLE TRACKING

The flow simulation algorithm was coupled with Lagrangian tracking. The equation of particle motion is given by

$$\frac{d^2\vec{r}'}{dt'^2} = \vec{a}'(\vec{v}', \vec{u}'), \tag{6}$$

where $\vec{r}'$ is the location of the particle and $\vec{a}'$ is its acceleration, which depends on the particle velocity $\vec{v}'$ and on the fluid velocity $\vec{u}'$.

The importance of the forces acting on particles in laminar and turbulent flow, which contribute to its acceleration, is a topic of recent discussions. Armenio and Fiorotto (2001), for example, analysed the importance of forces acting on a particle for different particle over fluid density ratios. We considered the equation for particle acceleration as was given by Maxey and Riley (1983):

$$\frac{d\vec{v}'}{dt'} = \vec{g} - \frac{\rho}{\rho_p}\vec{g} + \frac{\vec{u}' - \vec{v}'}{\tau_p} + \frac{\rho}{\rho_p}\frac{D\vec{u}'}{Dt'} + \frac{\rho}{2\rho_p}\left(\frac{d\vec{u}'}{dt'} - \frac{d\vec{v}'}{dt'}\right), \tag{7}$$

where $d/dt' = \partial/\partial t' + (\vec{v}' \cdot \vec{\nabla})$ and $D/Dt' = \partial/\partial t' + (\vec{u}' \cdot \vec{\nabla})$. ρ is the fluid density. ρ_p, d_p, τ_p are the particle density, particle diameter and $\tau_p = \rho_p d_p^2/\rho 18\nu$ is the particle relaxation time, where ν is the fluid viscosity. The terms on the right hand side of equation (7) represent gravity, buoyancy, drag, pressure gradient term and added mass. The equation is rewritten in non-dimensional form with u_0 and L being characteristic fluid velocity scale and characteristic problem length scale, yielding $\vec{u} = \vec{u}'/u_0$, $\vec{v} = \vec{v}'/u_0$, $t = t'u_0/L$:

$$\vec{a} = \frac{d\vec{v}}{dt} = \frac{A}{St}\{\vec{v}_s + \vec{u} - \vec{v}\} + \frac{3}{2}R\frac{\partial\vec{u}}{\partial t} + R\{(\vec{u} + \frac{1}{2}\vec{v}) \cdot \vec{\nabla}\}\vec{u}, \tag{8}$$

where the Stokes number is defined as

$$St = \frac{\rho_p d_p^2 u_0}{\rho 18\nu L}, \tag{9}$$

the settling velocity is

$$\vec{v}_s = \frac{d_p^2}{18\nu u_0}\left(\frac{\rho_p}{\rho} - 1\right)\vec{g} \tag{10}$$

parameters R and A are

$$R = \frac{\rho}{\rho_p + \frac{1}{2}\rho}, \qquad A = \frac{\rho_p}{\rho_p + \frac{1}{2}\rho}. \tag{11}$$

In the case of very light particles ($\rho_p \ll \rho$, bubble limit) the parameters R and A tend to $R \to 2$, $A \to 0$. In the aerosol limit ($\rho_p \gg \rho$), the parameters are $R \to 0$, $A \to 1$, rendering the pressure gradient and added mass terms negligible. For fluid particles ($\rho_p = \rho$), we have $R = A = 2/3$.

With the acceleration of the particle given in equation (8) we may solve the particle equation of motion (6) by employing the 4^{th} order Runge-Kutta method (Press *et al.* 1997).We integrate the following six equations simultaneously:

$$\frac{dx}{dt} = v_x, \quad \frac{dv_x}{dt} = a_x, \quad \frac{dy}{dt} = v_y,$$
$$\frac{dv_y}{dt} = a_y \quad \frac{dz}{dt} = v_z, \quad \frac{dv_z}{dt} = a_z. \tag{12}$$

The unknowns are the particle location x, y, z and particle velocity v_x, v_y, v_z. The initial particle location and velocity must be known. We require a subroutine calculating the right hand sides of the six equations. In order to calculate the acceleration on the right hand side, the velocity of the fluid $\vec{u}$ at the location of the particle is needed.

Flow simulations were performed on a mesh consisting of hexahedral elements. The first task to be performed in order to find the velocity of the fluid at the location of the particle is to find the mesh element in which the particle resides. This problem has been considered by Zhou and Leschziner (1999) as well as by Cheng *et al.* (1996). We used the technique proposed by Marchioli *et al.* (2007). We calculate outward pointing normal of each face of the mesh element. Then, we calculate dot product between the normal and vector connecting the element face and the particle location; $\vec{r} \cdot \vec{n}$. If dot products for all element faces are negative, then the particle is located in the element. See Fig. 4.

To avoid searching through the whole grid, the algorithm examines the mesh element in which the particle was located in the previous time step, secondly examines elements neighbouring this element and finally loops through all elements. When using adequate time steps, looping through all elements is necessary only in the case when particle leaves the computational domain. The proposed method works only for convex elements.

The next step is to interpolate the fluid velocity, which is known in the element's nodes, to the location of the particle. The solution of this problem in 2D was given in Ravnik *et. al* (2008)

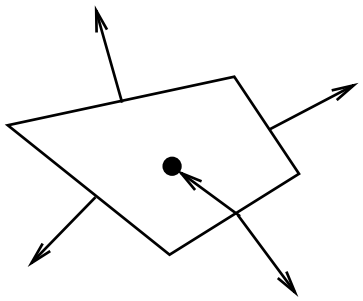

Fig. 5. A 2D representation of a hexahedral mesh element. Element face normals $\vec{n}$ and particle position vector $\vec{r}$ are shown.

and for 3D curvilinear grids by Marchioli *et al.* (2007). We extended the algorithm proposed in Ravnik *et. al* (2008) to three dimensions.

Consider single element in a mesh made out of arbitrary six sided parallelepipedial elements and its counterpart in the local coordinate system (Fig. 6).

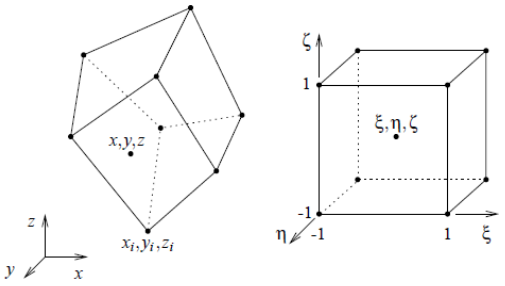

Fig. 6. A 3D representation of a hexahedral mesh element and its counterpart in the local coordinate system.

A point inside the element (x, y, z) may be written in local coordinate system (ξ, η, ζ) by using shape functions $\Phi_i(\xi, \eta, \zeta) = f(1, \xi, \eta, \zeta, \xi\eta, \xi\zeta, \eta\zeta)$ as

$$x(\xi, \eta, \zeta) = \sum_{i=1}^{8} \Phi_i(\xi, \eta, \zeta) x_i, \tag{13}$$

$$y(\xi, \eta, \zeta) = \sum_{i=1}^{8} \Phi_i(\xi, \eta, \zeta) y_i, \tag{14}$$

$$z(\xi, \eta, \zeta) = \sum_{i=1}^{8} \Phi_i(\xi, \eta, \zeta) z_i. \tag{15}$$

We are interested in exactly the inverse transformation; based on a known location (x, y, z) find the coordinates (ξ, η, ζ) in the local coordinate system. When (ξ, η, ζ) are known, we can interpolate any field function, which was the result of a CFD simulation, to the location (x, y, z).

Analytical solution for (ξ,η,ζ) given (x,y,z) for the above system of equations can not be found. The problem is solved numerically with the Newton-Raphson method (Press *et al.* 1997). The method uses first order Taylor expansion to write a linear system of equations for corrections of each unknown variable. Iteratively, the initial guesses for (ξ,η,ζ) are advanced towards the correct values. About a hundred iterations are needed to converge the solution to accuracy of 10^{-6}. This part of the particle tracking algorithm requires most CPU time.

The particle tracking algorithm can be summarized in the following points.

- Before simulation, pre-process mesh connectivity to make lists of neighbours for each mesh element. This greatly speeds up finding of the mesh element within which the particle is located.
- Use the element face normal times particle location dot product to find the mesh element within which the particle is located. Remember the particle's element of the previous time step. Check it and its neighbours first.
- Use the Newton-Raphson method to determine the velocity of the fluid at the location of the particle.
- Use the fourth order Runge-Kutta method to advance the particle location and velocity through time.

The derived algorithm has been used by Ravnik and Hriberšek (2013) and Ravnik *et al.* (2014) to simulate particle behaviour under the influence of magnetic forces.

4. CODE VALIDATION

4.1 Particle Tracking

Maxey (1987) studied the motion of small spherical particles in a cellular flow field. The study revealed the possibility that the particles remain suspended indefinitely in the flow field, a phenomenon which was observed while studying plankton movement. The problem was revisited recently by Marchioli *et al.* (2007), who provided additional results. Thus, particle movement patterns for the whole range of density ratios and Stokes numbers are available.

In order to validate our code, we repeated the experiment. The domain is given by $\Omega = [0,1]\times[0,1]$ and the flow field is

$$\vec{u} = \left\{ \begin{array}{c} \sin 2\pi x \cos 2\pi z \\ 0 \\ \cos 2\pi x \sin 2\pi z \end{array} \right\},$$
$$\vec{\omega} = \left\{ \begin{array}{c} 0 \\ 4\pi \sin 2\pi x \sin 2\pi z \\ 0 \end{array} \right\}, \qquad (16)$$

while gravity acts in negative z direction; $\vec{g} = (0,0,-9.81 m/s)$. The flow field is shown in Figure 7. Since our code is 3D, we made the mesh only 1 element deep. The flow field is periodic, thus particles exiting the domain on one side are put back into the domain on the opposite side. In order to properly test the code, we used the analytical equation (16) to calculate velocities in nodes of a uniform $25\times1\times25$ element mesh. The total number of nodes was 7803. The fluid velocity at the location of the particle was, during tracking, interpolated using the technique described in section 3. and was not calculated analytically using equation (16).

For a vapour bubble, Maxey (1987) introduced two more nondimensional parameters: the rise velocity $Q = -v_s^z/(1/R - 3/2)$ and the inertia parameter $B = 2\frac{A}{St}/R$.

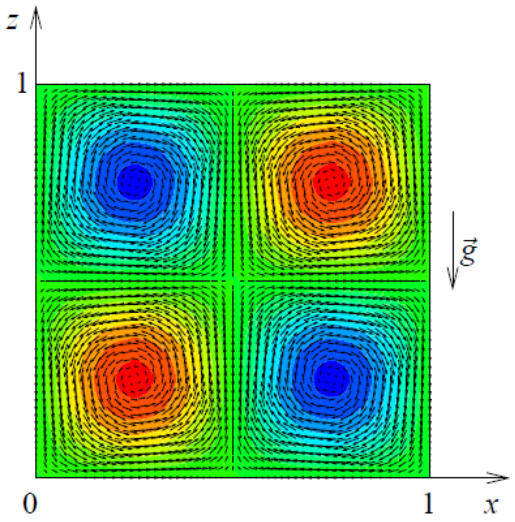

Fig. 7. Cellular flow field. Velocity vectors and vorticity contours are shown. Red colour indicates anticlockwise rotating vortices, blue colour indicates clockwise rotating vortices.

First we consider the bubble limit, i.e. particle density is much less than the fluid density $\rho_p \ll \rho_f$. The following parameters were chosen for simulation: $A/St = 10$, $R = 2$, $v_s^z = 0.8$, $Q = 0.8$, $B = 10$. A thousand particles were inserted into the flow field at random locations

and were given the velocity equal to the velocity of the fluid at that location. We let the simulation run and discovered, that all of the particles are trapped and converge to equilibrium locations in the flow field. Particle collisions were not considered, thus all particles end up at the same locations after a long time. Figure 8 shows the flow field with particles at the start of the simulation and at two later times.

If we increase the settling velocity to $v_s^z = 1.25$ and keep all other parameters the same, we observe (Figure 9) that the particles are now able to escape the vortices and move upwards on trajectories only partially affected by the flow field.

Next, we increased the particle density to one half of the fluid density. When studying particle movement in the transition range between the bubble limit and the aerosol limit ($0.4 < R < 2$), it is appropriate to assign a fixed value to Q and B while R is varied. Thus in order to keep B and Q fixed, the parameters are: $\rho_p = \frac{1}{2}\rho_f$, $A/St = 5$, $R = 1$, $v_s^z = 0.625$, $B = 10$, $Q = 1.25$. The results in Figure 10 show that in this case, some particles are captured within the vortices, while others manage to circumvent the vortices.

Increasing the particles density even further, we simulated particles with density $\rho_p = 0.928\rho_f$. The results in Figure 11 show that most of the particles are captured near to the centre of the vortices and only some are able to circumvent the vortices.

Next, we set the particle density to be a little larger than the fluid density ($\rho_p = 1.1666\rho_f$). The settling velocity changes sign, the particles move downwards. This slight change of density causes the particles to be thrown out of vortices instead of being captured by vortices as in the $\rho_p = 0.928\rho_f$ case. Flow field and particle locations are shown in Figure 12. The transition occurs when parameter R becomes smaller than $R < 2/3$.

The behaviour of particles and the conclusions of our analysis are equivalent to the findings of Maxey (1987) and Marchioli *et al.* (2007), thus validating our particle tracking algorithm.

5. PARTICLE TRACKING IN A LID DRIVEN CAVITY

Study of behaviour of particles in lid driven cavity flows a topic of recent research. Kosinski et al. Kosinski *et al.* (2009) numerically studied behaviour of dust clouds taking into account particle-particle interactions and two-way coupling. Tsorng *et al.* (2008) studied behaviour of macroscopic rigid particles suspended in a fully three-dimensional lid driven cavity flow field. They used 2D PIV experimental technique to examine the particle motion. Our aim was to repeat and extend these experiments using the developed numerical technique. Tsorng *et al.* (2008) reported most of their findings at $Re = 470$ and some at $Re = 130$ and $Re = 860$. We chose the same Reynolds numbers for our numerical experiments. We used micro particles to visualize the flow fields. Motion of slightly buoyant and non-buoyant macro particles was investigated next. The particle diameter was varied in order to investigate, if the particles are able to enter into secondary vortices.

Particle boundary condition on the walls of the cavity was implemented as an elastic collision. A particle which is, after a time step, found outside of the problem domain, is mirrored back inside into the domain. Its velocity is also mirrored across a plane tangential to the wall.

5.1 Micro Particles

If one considers particles with very small diameter having density equal to the density of the fluid, the resulting Stokes number is very low. Particles respond to the changes of the flow field very quickly and manage to follow the fluid streamlines very closely.

Micro particles were simulated in a $L = 10cm$ square cavity, which was filled with fluid with density $\rho = 1500kg/m^3$ and viscosity $\nu = 37.2mm^2/s$. Particle diameter was $d_p = 10\mu m$ and its density was equal to the fluid density; $\rho_p = \rho = 1500kg/m^3$. The chosen fluid to particle density ratio gives, according to equation (11), the following values for parameters $A = R = 2/3$ as well as renders the settling velocity zero; $v_s = 0$. The lid driving velocity u_0 was chosen in such manner that the flow Reynolds number values $Re = Lu_0/\nu$ reached the values of 130, 470, and 860. Table 1 lists the lid velocities and Stokes numbers for the three cases

Table 1 Parameters used for Lagrangian particle tracking in lid driven cavity - case of micro particles. Fluid properties: $\rho = 1500kg/m^3$, $\nu = 37.2mm^2/s$; **particle data:** $d_p = 10\mu m$, $\rho_p = 1500kg/m^3$; **cavity size** $L = 10cm$; **equation of motion (??) parameters:** $A = R = 2/3$, $v_s = 0$

case	Re	$u_0[mm/s]$	St
g)	130	48.36	$0.7 \cdot 10^{-7}$
h)	470	174.84	$2.6 \cdot 10^{-7}$
i)	860	319.92	$4.8 \cdot 10^{-7}$

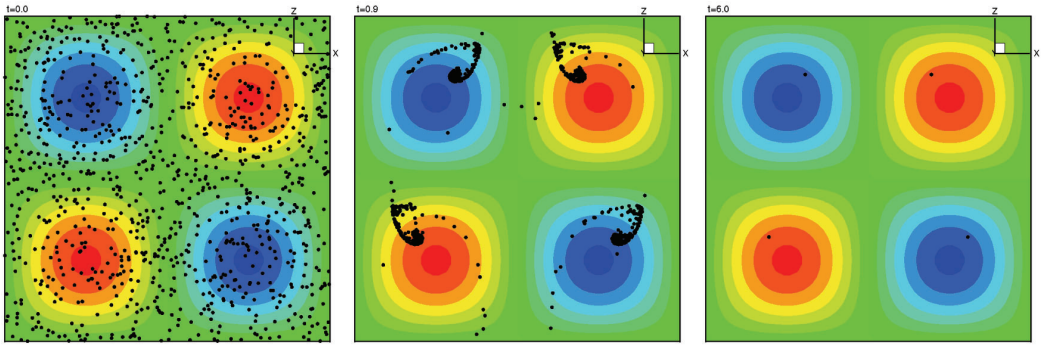

Fig. 8. Simulation of bubbles in a cellular flow field; $\rho_p \ll \rho_f$, $A/St = 10$, $R = 2$, $v_s^z = 0.8$, $Q = 0.8$, $B = 10$**. Particle positions are shown at the beginning of the simulation (left) and at two later times.**

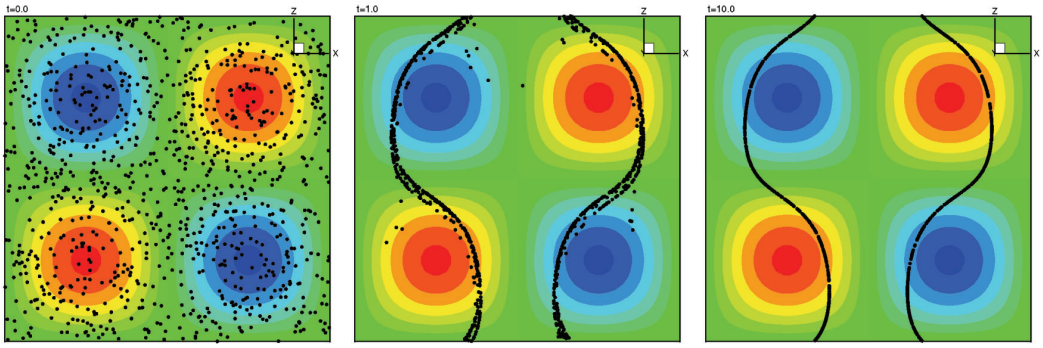

Fig. 9. Simulation of bubbles in a cellular flow field; $\rho_p \ll \rho_f$, $A/St = 10$, $R = 2$, $v_s^z = 1.25$, $B = 10$, $Q = 1.25$**.**

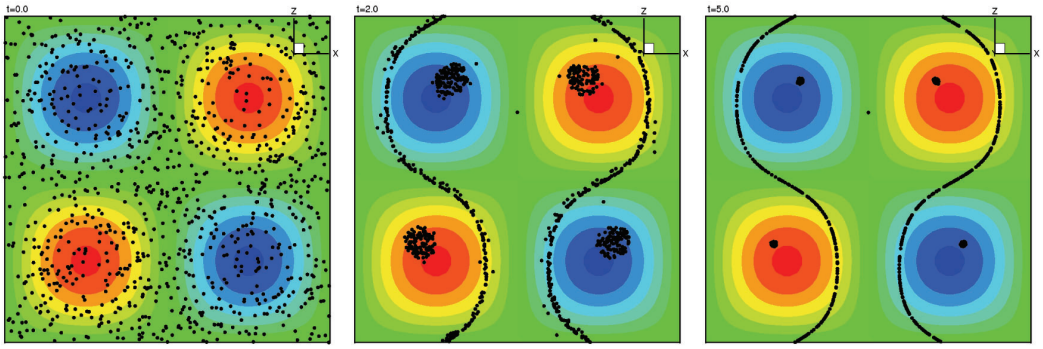

Fig. 10. Simulation of light particles in a cellular flow field; $\rho_p = \frac{1}{2}\rho_f$, $A/St = 5$, $R = 1$, $v_s^z = 0.625$, $B = 10$, $Q = 1.25$**.**

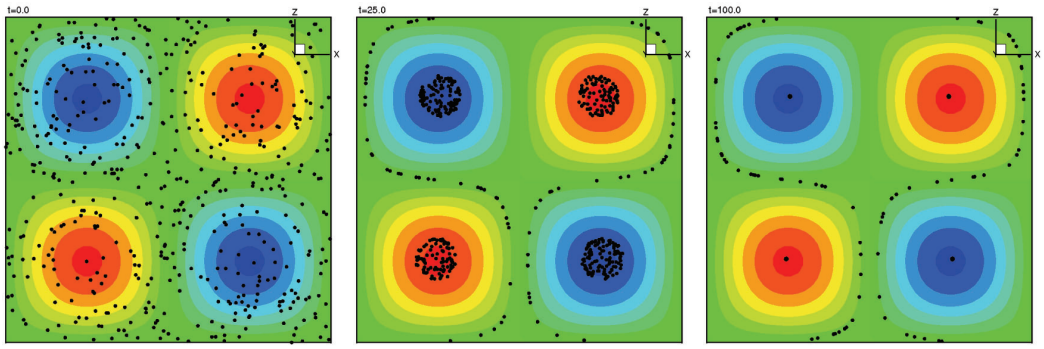

Fig. 11. Simulation of light particles in a cellular flow field; $\rho_p = 0.928\rho_f$, $A/St = 3.5$, $R = 0.7$, $v_s^z = 0.0892$, $B = 10$, $Q = 1.25$.

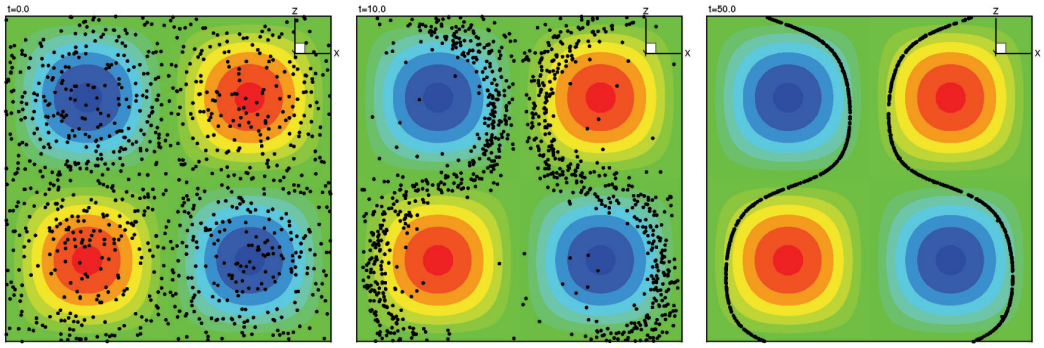

Fig. 12. Simulation of slightly heavy particles in a cellular flow field; $\rho_p = 1.1666\rho_f$, $A/St = 3$, $R = 0.6$, $v_s^z = -0.20833$, $B = 10$, $Q = 1.25$.

considered.

The results show that, as expected, the micro particles indeed follow the flow streamlines closely. Since the flow field is resolved in terms of velocity and vorticity fields, the streamlines field has to be computed as a post processing task. Flow streamlines were calculated by integrating the velocity flow field using the Tecplot visualisation software. Comparison of micro particle paths and flow streamlines presented in Figure 13 reveals particles movement along the streamline, starting in the primary vortex and heading into the secondary vortex in the lower part of the cavity. The particle was released into the flow at $(0.5, 0.5, 0.45)$ having the velocity of the fluid at that location.

5.2 Macro Particles

We consider macroscopic particles with diameter $d_p = 3mm$ in a $L = 10cm$ lid driven cavity. The particles density was $\rho_p = 1210kg/m^3$. The particles were inserted into two fluids. The density of the first fluid was $\rho = 1210.605kg/m^3$ making the particles slightly buoyant. The density of the second fluid was $\rho = 1209.153kg/m^3$ making the particles non-buoyant with a small settling velocity. Flow Reynolds numbers $Re = 130$, $Re = 470$ and $Re = 860$ were considered. Lists of Stokes numbers and lid driving velocities are given in Tables 2and 3.The simulation parameters were chosen such that the particle Stokes numbers are equal for both - buoyant and non-buoyant cases.

The comparison of macro particle paths and flow streamlines shows for both buoyant and non-buoyant case that for a certain time the particle follows flow streamline. After that, due to the reasonably large Stokes number, the particle path deviates from the streamline, which after a long time results in a particle trajectory, which has no correlation with the flow streamline. Figure 13 confirms this findings by comparing flow streamline and a trajectory of a single particle, which was released into the flow at $(0.5, 0.5, 0.45)$. Initially the particle velocity was set to be equal to the flow velocity.

Examination of the flow field shows, that they are symmetrical across the $y = 0.5$ plane for the Reynolds numbers considered in this paper. In order to examine how the macro particles behave in the vortical structure of the flow field, we inserted a single particle at $(0.5, 0.4, 0.45)$. Figure 14 shows the trajectory for the non-

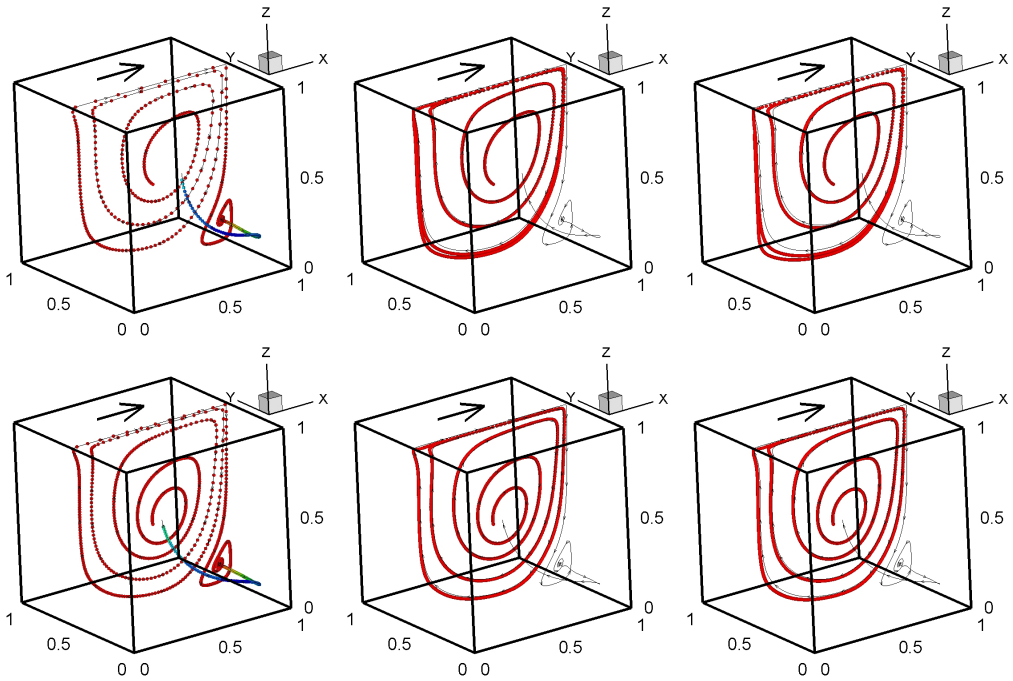

Fig. 13. Comparison of particle paths and flow streamlines in a lid driven cavity. The particles were released into the flow at $(0.5, 0.5, 0.45)$ having the velocity of the fluid at that location. Results in the top row $Re = 470$ and in the bottom row $Re = 860$. From left to right: micro particles, buoyant macro particles and non-buoyant macro particles.

buoyant case and Figure 15 shows trajectories for the buoyant case. We notice, common to all Reynolds number considered, that the particle trajectory remains in the large central primary vortex and does not reach secondary vortices in the corners of the cavity. The primary vortex is small in the case of $Re = 130$, thus accordingly, the particle remains mostly in the central upper half of the cavity. As the primary vortex grows in size when the Reynolds number is increased, the particle is able to penetrate all parts of the cavity except the secondary vortices in the lower corners. Symmetry of the flow field is confirmed by the fact that none of the particles is able to cross the plane at $y = 0.5$ and remains on one side of the cavity at all times.

5.3 Particles in Secondary Corners

Tsorng *et al.* (2008) examined the reasons for the fact that the macro ($d_p = 3mm$) particles remain entrained in the primary vortex and do not enter the secondary corner vortices. They argued that the particle size (i.e. diameter) is the crucial factor for this behaviour considering the chosen particle and fluid densities. By examining the flow field, they observed that only a narrow streamline corridor close to the top ($z = 1$) and right walls ($x = 1$) lead to the secondary vortices. They concluded that the $3mm$ particles were too large to enter this corridor and thus do not enter the secondary corner vortices. Their findings are verified by careful experimental work, whereas they only used a CFD approach for simulation of micro (fluid) particles paths, which were identical to fluid streamlines.

In order to complete the comparison, we examined the remaining situations using previously described and verified numerical algorithm for flow simulation and particles tracking. We inserted 1000 particles into flow fields. Initially, particles were randomly distributed within a cube in the centre of the cavity $(0.3 < x, y, z < 0.7)$. Particle diameter was varied between $0.3mm$ and $2mm$, since we have already confirmed in previous section, that $3mm$ particles do not enter the secondary vortices.

We considered two secondary vortices. The right secondary vortex is considered to be in the bottom right region of the cavity, i.e. where $x \approx 1$ and $z \approx 0$, while the left secondary vortex is in the bottom left part of the cavity, i.e. where $x \approx 0$ and $z \approx 0$. Locations of secondary vortices are schematically shown in Figure 2. Results of entrainment of particles into secondary vortices are shown in Table 4 and described below.

At $Re = 130$ we observed that regardless of the diameter size, none of the buoyant particles en-

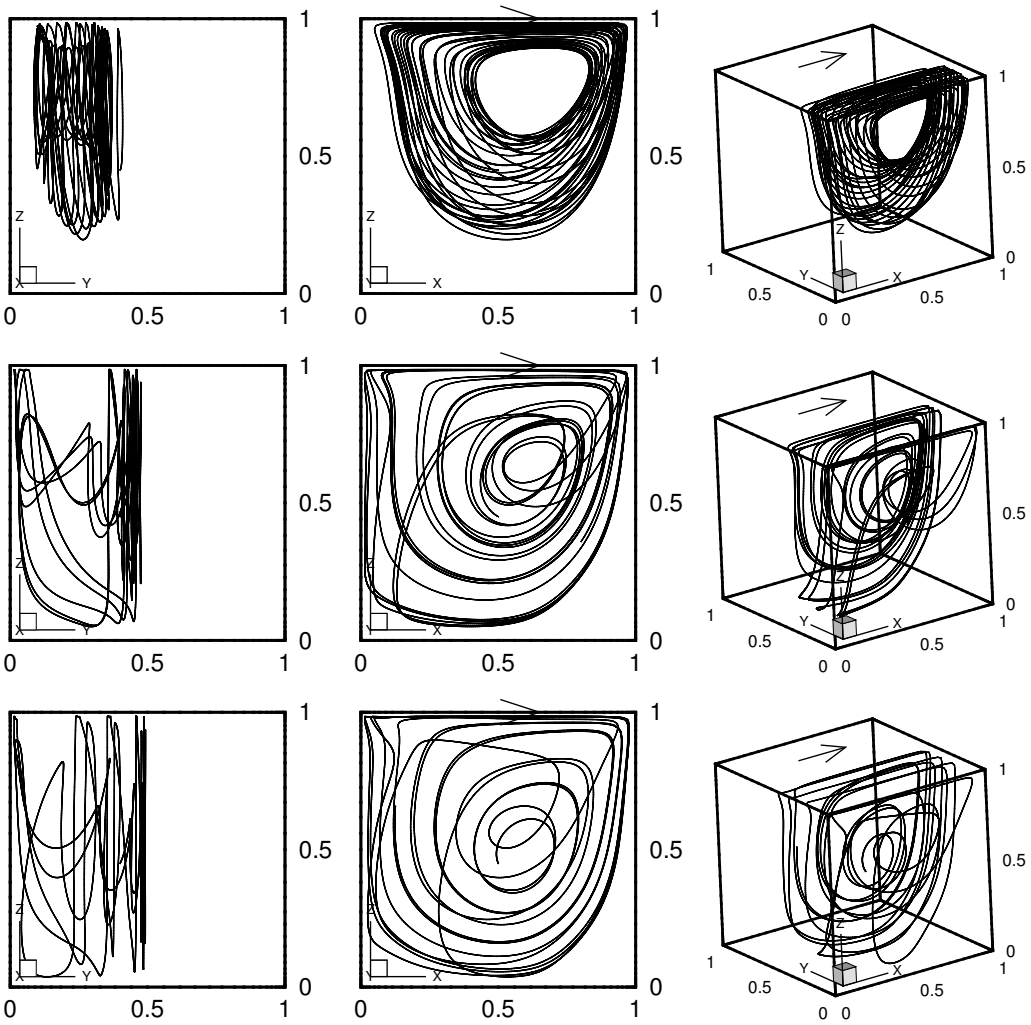

Fig. 14. Trajectory of a non-buoyant macro particle released into the flow at $(0.5, 0.4, 0.45)$ **for** $Re = 130$ **(top),** $Re = 470$ **(middle) and** $Re = 860$ **(bottom). Table 5.3 provides all parameters of the simulation**

Table 2 Parameters used for Lagrangian particle tracking in lid driven cavity - case of non-buoyant macro particles. Fluid properties: $\rho = 1209.153 kg/m^3$**,** $\nu = 17.3 mm^2/s$**; particle data:** $d_p = 3mm$**,** $\rho_p = 1210 kg/m^3$**; cavity size** $L = 10cm$**; equation of motion (8) parameters:** $A = 0.666822259$**,** $R = 0.666355483$**,** $v_s = -0.19 mm/s$

case	Re	$u_0[mm/s]$	St
d)	130	22.49	$6.50 \cdot 10^{-3}$
e)	470	81.31	$23.51 \cdot 10^{-3}$
f)	860	148.78	$43.03 \cdot 10^{-3}$

Table 3 Parameters used for Lagrangian particle tracking in lid driven cavity - case of slightly buoyant macro particles. Fluid properties: $\rho = 1210.6053 kg/m^3$**,** $\nu = 37.2 mm^2/s$**; particle data:** $d_p = 3mm$**,** $\rho_p = 1210 kg/m^3$**; cavity size** $L = 10cm$**; equation of motion (8) parameters:** $A = 0.666555519$**,** $R = 0.666888963$**,** $v_s = 0.0659 mm/s$

case	Re	$u_0[mm/s]$	St
a)	130	48.36	$6.49 \cdot 10^{-3}$
b)	470	174.84	$23.49 \cdot 10^{-3}$
c)	860	319.92	$42.97 \cdot 10^{-3}$

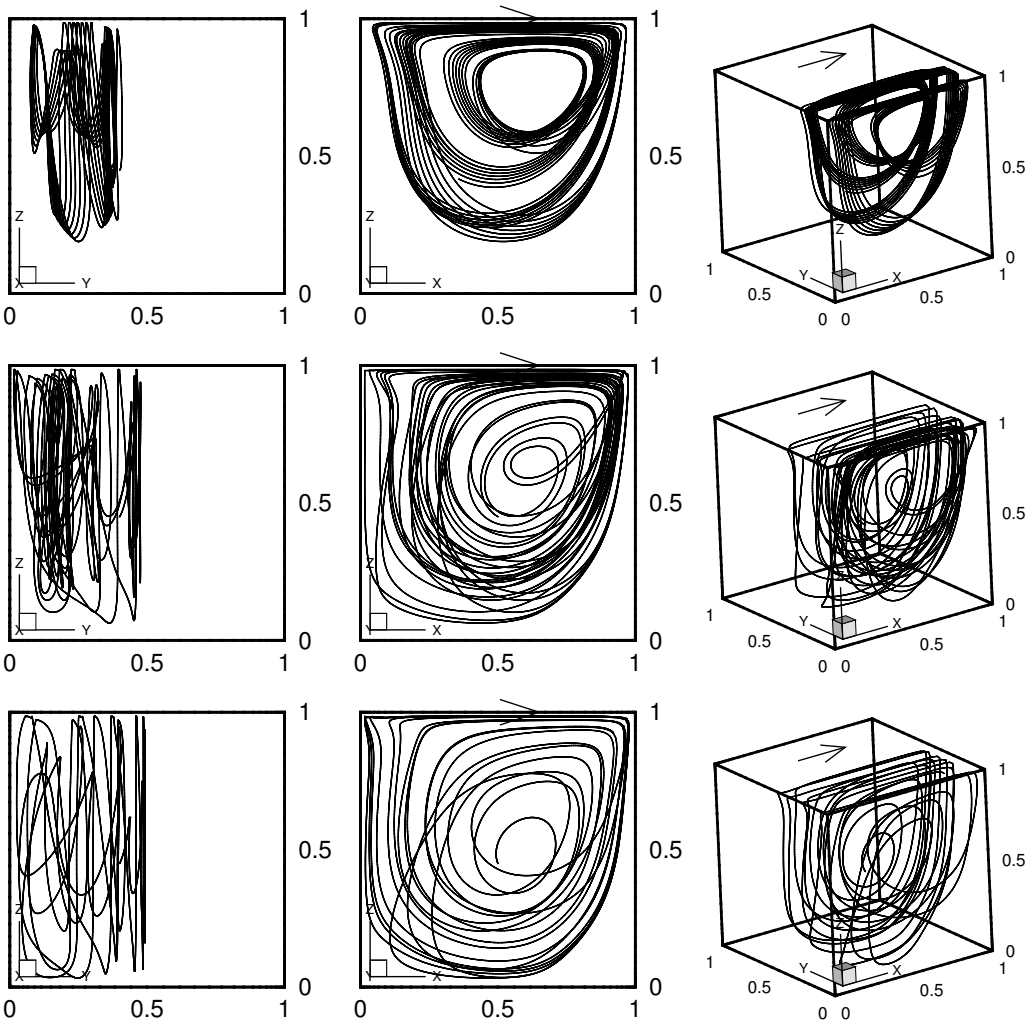

Fig. 15. Trajectory of a buoyant macro particle released into the flow at $(0.5, 0.4, 0.45)$ **for** $Re = 130$ **(top),** $Re = 470$ **(middle) and** $Re = 860$ **(bottom). Table 5.3 provides all parameters of the simulation.**

ter the secondary vortices. Particles with a small diameter can be found throughout the primary vortex. Particles with a larger diameter move closer to the vortex core, but none actually enter the core (Figure 16).

Non-buoyant particles at $Re = 130$ with diameters less than $d_p \leq 0.5mm$ do not enter the secondary vortices. Most of the particles remain entrapped in the primary vortex, while some settle on the ground of the cavity. Particles with larger diameters enter the left secondary vortex, but they are not entrapped within. The larger the particle diameter, the more particles settle on the ground. None of the particles are able to enter the right secondary vortex.

Buoyant particles at $Re = 470$ with small diameter $d_p \leq 0.75mm$ enter the secondary vortices. Most of them enter the right vortex around the central plane. An interesting phenomenon occurs with $d_p = 1mm$ particles. Although they do not enter the core of the right secondary vortex around the central $y = 0.5$ plane, they are sucked into the right corners of the cavity. Cavity with particle positions demonstrating this effect is shown in Figure 17. Particles with diameters $d_p = 1.25mm$ and $d_p = 1.5mm$ enter only the left vortex, while $d_p = 2mm$ particles do not enter any of the secondary vortices.

Non-buoyant particles at $Re = 470$ with small diameter $d_p \leq 0.75mm$ enter the secondary vortices after first making a few revolutions in the main vortex. At $d_p = 0.75mm$ some particles settle on the ground of the cavity. At $d_p = 1mm$ the particles do not enter the right secondary vortex in the centre of the cavity, but do reach the corners of the cavity. However, since they are non-buoyant, they settle on the bottom of the cavity. Cavity with particle positions demon-

Table 4 Entrance of particles in secondary vortices in the bottom right and left part of the cavity. Particles do not enter the secondary vortices (-), particles enter both secondary vortices (+), (l) particles enter the left secondary vortex only

	$Re = 130$		$Re = 470$		$Re = 860$	
$d_p[mm]$	buoy.	non-buoy.	buoy.	non-buoy.	buoy.	non-buoy.
0.3	-	-	+	+	+	+
0.5	-	-	+	+	+	+
0.75	-	l	+	+	+	+
1.0	-	l	l	l	+	+
1.25	-	l	l	l	l	l
1.5	-	l	l	l	l	l
2.0	-	l	-	l	-	-

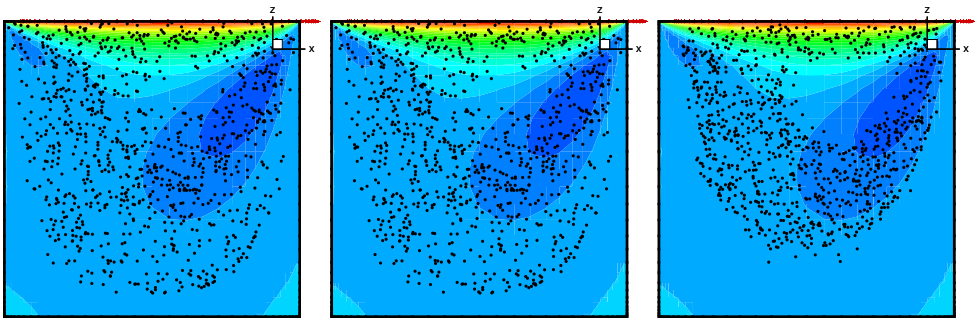

Fig. 16. Buoyant particles with $d_p = 0.3mm$ (left), $d_p = 1mm$ (middle) and $d_p = 2mm$ (right) at $Re = 130$ after a long time shown on the $x-z$ plane. None of the particles enter the secondary vortices. Smaller particles find their way into the whole primary vortex, while larger are kept in a torus shape by the flow. Contours of u_x flow velocity component are shown in a slice at $y = 0.94$.

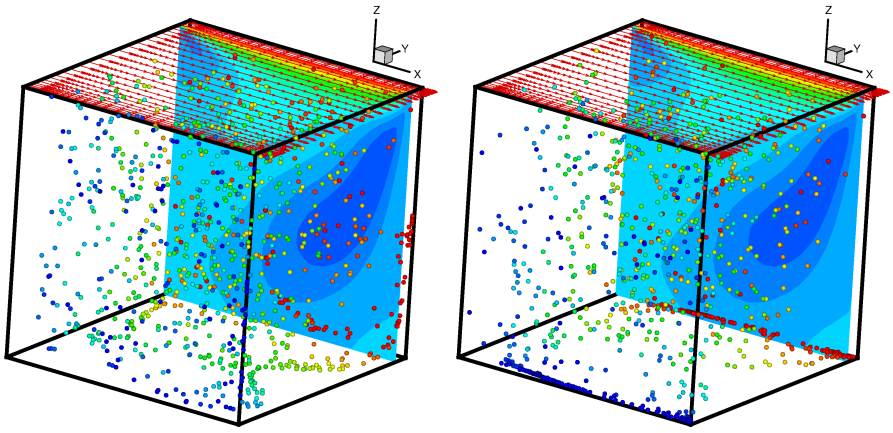

Fig. 17. Buoyant (left) and non-buoyant (right) $d_p = 1mm$ particle positions after a long time in a cavity at $Re = 470$. None of the particles enter the right secondary vortex at $x = 1$, $y = 0.5$, while they are entrained into both $x = 1$ corners. Particle colour refers to its y coordinate. Contours of u_x flow velocity component are shown in a slice at $y = 0.94$.

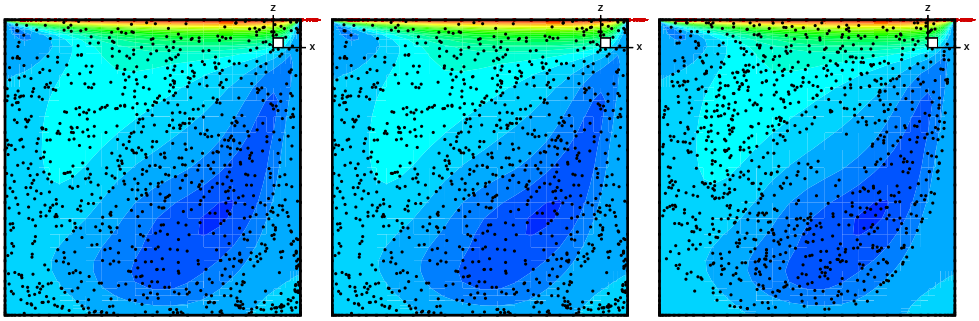

Fig. 18. Buoyant particles with $d_p = 1mm$ (left), $d_p = 1.5mm$ (middle) and $d_p = 2mm$ (right) at $Re = 860$ after a long time shown on the $x-z$ plane. While the small particles enter both secondary vortices, the middle size particles enter only the left secondary vortex and the large particles do not enter any. Contours of u_x flow velocity component are shown in a slice at $y = 0.94$.

strating this effect is shown in Figure 17. Particles with diameter $d_p \geq 1.25mm$ enter only the left secondary vortex. Some of the particles, which enter the left secondary vortex, settle to the ground. As the particle diameter increases the number of particles entering the left vortex and the number of particles settling to the ground diminishes.

Buoyant particles at $Re = 860$ with diameters $d_p \leq 1mm$ enter the secondary vortices and can be, after a long time, found in the whole cavity. For $d_p = 1.25mm$ and $d_p = 1.5mm$ particles can be found only in the left secondary vortex, while none enter the right vortex. At $d_p = 2mm$ all particles remain in the primary vortex (Figure 18).

Small non-buoyant particles at $Re = 860$ enter both secondary vortices when their diameter is less than $d_p \leq 1mm$. There is no settling of particles with $d_p = 0.3mm$. With increasing diameter more and more particles settle on the ground. At $d_p = 1.25mm$ and $d_p = 1.5mm$ the particles are able to reach only the left secondary vortex. Most of the particles, which enter the secondary vortex, settle to the ground. However at $d_p = 2mm$ no settling occurs at all. All of the particles are kept in the primary vortex, none enter the secondary vortices and none settle to the ground.

In summary, we discovered that only particles with diameters below a certain limit are able to enter in both secondary vortices. This limit depends on the Reynolds number. Particles with diameters above this limit are able to enter into the left secondary vortex only. As the particle diameter is increased even further, all particles remain in the primary vortex. The difference between buoyant and non-buoyant particles is expressed above all in the fact that the non-buoyant particles tend to settle to the ground. Since the secondary vortices are located at the bottom of the cavity, the non-buoyant particles are able to enter the secondary vortices with higher diameters than the buoyant particles.

6. CONCLUSIONS

A Lagrangian particle tracking algorithm was presented for simulation of dilute suspensions of particles in viscous flow. The physical model includes gravity, buoyancy, drag, pressure gradient and added mass effects. The particle equation of motion was solved and advanced through time by the Runge-Kutta method. Interpolation of fluid velocity to the location of the particle in the computational mesh was done by solving a non-linear system of equations using the Newton-Raphson method. Boundary element method based numerical algorithm for the solution of velocity-vorticity form of Navier-Stokes equations was used to simulate viscous flow.

The particle tracking code was validated by revisiting a problem of particle movement in a cellular flow field. Very good agreement between present results and previously published results of other authors was observed.

The developed algorithm was used to study the behaviour of macroscopic slightly buoyant and slightly non-buoyant particles in a lid driven cavity. The flow in a lid driven cavity is fully three-dimensional and features a primary vortex in the main part of the cavity as well as secondary vortices in the corners of the cavity. We investigated the particle movement and discovered, that particles above a certain size, can not enter secondary vortices. The size limit increases with Reynolds number value. For the selected diameter data range, in case of $Re =$

470 the limit is $d_p = 0.75$mm, and in case of $Re = 860$ the limit is $d_p = 1.0$mm, both limits valid for the case of entering both secondary vortices. The physical reason for such behaviour was found to be the flow structure. Only small streamline paths lead to the secondary vortices, which can not be entered by larger particles. Thus the larger particles remain trapped in the primary vortex, while smaller particles are able to enter into the secondary vortices in the corners of the cavity.

REFERENCES

Armenio, V. and V. Fiorotto (2001). The importance of the forces acting on particles in turbulent flows. *Phys. Fluids 13*, 2437–2440.

Cheng, H.-P., J.-R. Chend and G.-T. Yeh (1996). A particle tracking technique for the Lagrangian-Eulerian finite element method in multi-dimensions. *Int. J. Numer. Meth. Engng. 39*, 1115–1136.

Crowe, C. T., M. Sommerfeld and Y. Tsuji (1998). *Multiphase flows with droplets and particles*. CRC press.

Kosinski, P., A. Kosinska and A. Hoffmann (2009). Simulation of solid particles behaviour in a driven cavity flow. *Powder Technology 191*, 327–339.

Marchioli, C., V. Armenio and A. Soldati (2007). Simple and accurate scheme for fluid velocity interpolation for Eulerian-Lagrangian computation of dispersed flows in 3D curvilinear grids. *Comput. & Fluids 36*, 1187–1198.

Marchioli, C., M. Fantoni and A. Soldati (2007). Influence of added mass on anomalous high rise velocity of light particles in cellular flow field. A note on the paper of Maxey (1987). *Phys. Fluids, 19*, 098101.

Maxey, M. (1987). The motion of small spherical particles in a cellular flow field. *Phys. Fluids 30*, 1915–1928.

Maxey, M. and J. Riley (1983). Equation of motion for a small rigid sphere in a nonuniform flow. *Phys. Fluids 26*, 883–889.

Mendez, Y. (2011). A flow model for the settling velocities of non spherical particles in creeping motion. *Journal of Applied Fluid Mechanics 4*, 65–75.

Necker, F., C. Härtel, L. Kleiser and E. Meiburg (2002). High-resolution simulations of particle-driven gravity currents. *Int. J. Multiphase Flow 28*, 279–300.

Paige, C. C. and M. A. Saunders (1982). LSQR: An algorithm for sparse linear equations and sparse least squares. *ACM Transactions on Mathematical Software 8*, 43–71.

Patankar, N. and D. Joseph (2001). Lagrangian numerical simulation of particulate flows. *Int. J. Multiphase Flow 27*, 1685–1706.

Press, W. H., S. A. Teukolsky, W. T. Vetterling and B. P. Flannery (1997). *Numerical Recipes − The Art of Scientific computing, Second Edition*. Cambridge University Press.

Ravnik, J. and M. Hriberšek (2013). High gradient magnetic particle separation in viscous flows by 3D BEM. *Comput Mech 51*, 465–474.

Ravnik, J., M. Hriberšek, F. Vogel and P. Steinmann (2014). Numerical simulation of particles movement in cellular flows under the influence of magnetic forces. *Int. J. Simul. Model 3*, 300–311.

Ravnik, J., L. Škerget, M. Hriberšek and Z. Žunič (2008). Numerical simulation of dilute particle laden flows by wavelet BEM-FEM. *Comput. Meth. Appl. Mech. Engrg. 197/6-8*, 789–805.

Ravnik, J., L. Škerget and Z. Žunič (2008). Velocity-vorticity formulation for 3D natural convection in an inclined enclosure by BEM. *Int. J. Heat Mass Transfer 51*, 4517–4527.

Ravnik, J., L. Škerget and Z. Žunič (2009). Combined single domain and subdomain BEM for 3D laminar viscous flow. *Eng. Anal. Bound. Elem. 33*, 420–424.

Razmi, A., B. Firoozabadi and G. Ahmadi (2009). Experimental and numerical approach to enlargement of performance of primary settling tanks. *Journal of Applied Fluid Mechanics 2*, 1–12.

Sachdev, J., C. Groth and J. Gottlieb (2007). Numerical solution scheme for inert, disperse, and dilute gas-particle flows. *Int. J. Multiphase Flow 33*, 282–299.

Škerget, L., M. Hriberšek and Z. Žunič (2003). Natural convection flows in complex cavities by BEM. *Int. J. Num. Meth. Heat & Fluid Fl. 13*, 720–735.

Tamayol, A., B. Firoozabadi and G. Ahmadi (2008). Determination of settling tanks performance using an eulerian-lagrangian method. *Journal of Applied Fluid Mechanics 1*, 43–54.

Tsorng, S. J., H. Capart, D. Lo, J. Lai and D. Young (2008). Behaviour of macroscopic rigid spheres in lid-driven cavity flow. *Int. J. Multiphase Flow 34*, 76–101.

van Wachem, B. and A. Almstedt (2003). Methods for multiphase computational fluid dynamics. *Chemical Engineering Journal 96*, 81–98.

Zhou, Q. and M. Leschziner (1999). An improved particle-locating algorithm for eulerian-lagrangian computations of two-phase flows in general coordinates. *Int. J. Multiphase Flow 25*, 813–825.